Systematic experimental and model-based evaluation of the synergistic effects of alloy composition and damage rate on the formation of Cr-rich precipitates in Fe–Cr–Al alloys under ion irradiation

Y. Abe[a], T.T. Sasaki[b], S. Yamashita[a], N. Okubo[a], S. Ukai[a,c]

[a] *Japan Atomic Energy Agency, 2-4 Shirakata, Tokai-mura, Ibaraki, 319-1195, Japan*
[b] *Research Center for Magnetic and Spintronic Materials, National Institute for Materials Science, 1-2-1 Sengen, Tsukuba, Ibaraki, 305-0047, Japan*
[c] *Hokkaido University, Kita 13, Nishi 8, Kita-ku, Sapporo, 060-8628, Japan*

Abstract

Fourteen Fe–Cr–Al alloys with systematically varied Cr and Al compositions were irradiated at 350°C to 0.24 dpa by 10.5 MeV self-ions as model alloys for the Fe–Cr–Al (oxide dispersion strengthened: ODS) alloys being developed as accident tolerant fuel (ATF) cladding for light water reactors. Three dose rates (8×10^{-6}, 8×10^{-5}, and 8×10^{-4} dpa/s) were selected to predict the formation behavior of Cr-rich precipitates (CrRP) under neutron irradiation conditions. The effects of Cr, Al composition, and dose rate on the CrRP formation behavior were evaluated using a three-dimensional atom probe (3DAP) analysis. The results showed that the CrRP number density, volume fraction, and Cr concentration increase with increasing Cr composition, decreasing Al composition, and decreasing dose rate. Multiple regression analysis showed that in addition to these primary effects, there was an interaction between them on the CrRP volume fraction: (1) the higher the Al composition, the smaller the increase in the CrRP volume fraction with increasing Cr composition, and (2) the lower the Cr composition, the smaller the increase in the CrRP volume fraction with the decreasing Al composition and dose rate. It was also highlighted that to understand the dose rate effect on the CrRP formation behavior under neutron irradiation, it is useful to examine the irradiation time dependence, including the effective use of thermal aging data as a limit to the zero dose rate, in addition to the the dose-dependency perspective. In addition to the systematic database of

CrRP-related quantities established in this study, these considerations should contribute to further developing and validating numerical prediction models.

Keywords: accident tolerant fuel (ATF) cladding, Fe–Cr–Al alloys, Cr-rich precipitate, ion irradiation, dose rate, 3D atom probe tomography

1. Introduction

Oxide dispersion-strengthened (ODS) Fe–Cr–Al alloys have been developed for early practical application in accident-tolerant fuel (ATF) cladding because the formation of an alumina protective layer by Al addition is effective in preventing steam oxidation during accidents [1]. Cr addition improves corrosion and oxidation resistance, but as Cr addition increases, α' phase/Cr-rich precipitates (CrRPs), which cause embrittlement, arise from the matrix (α phase). This is a known cause of the so-called 475°C embrittlement in the thermal aging of high Cr ($>$ 11 wt.%) ferritic/martensitic steels [2–4]. Under irradiation, the accumulation of irradiation defects and the associated formation of the CrRPs is the primary cause of irradiation embrittlement in Fe–Cr–Al alloys and is a design challenge.

In the thermal aging experiments of Kobayashi et al. [5], the increase in Vickers hardness was suppressed when Al was added to the Fe–Cr alloy, indicating that CrRP formation was suppressed. However, under neutron irradiation, CrRP formation was observed even in Fe–Cr–Al alloys with relatively high Al additions [6]. It has also been reported that the CrRP size increased and the number density decreased under neutron irradiation compared to ion irradiation in Fe–18Cr alloys [7]. CrRP formation under irradiation is strongly influenced by irradiation conditions such as temperature, irradiation rate, and dose. In particular, the dose rate effect on CrRP formation is influenced by the competition between diffusion enhancement by irradiation and ballistic dissolution by cascade damage [8, 9]. Modeling calculations considering the balance between these conflicting effects have been reported to predict the behavior of CrRP formation under irradiation in Fe–Cr alloys [10]. However, in Al-doped Fe–Cr–Al alloys, the elementary processes induced by irradiation should be more complex, and the control mechanisms for the formation and suppression of CrRPs, including the effect of Al addition under irradiation, are not yet fully understood. Irradiation experiments on Fe–Cr–Al alloys with systematically varied Cr and Al matrix compositions are essential to elucidate this.

However, from the viewpoint of promoting the technological demonstration of Fe–Cr–Al alloys, irradiation experiments on the ductility reduction due to CrRP formation under neutron irradiation conditions are necessary. However, the primary challenge is the limited number of irradiation reactors worldwide required to ensure safety in the high irradiation regime. As an alternative, accelerated irradiation tests using ion irradiation have shown promise. However, predicting the CrRP formation behavior in Fe–Cr–Al alloys under neutron irradiation (10^{-7}–10^{-6} dpa/s) from ion irradiation tests with dose rates at least two orders of magnitude higher is challenging. Therefore, it is essential to develop simulation and evaluation techniques to address complex environments in a unified manner by elucidating the CrRP formation behavior in Fe–Cr–Al alloys under different dose rates and systematically different alloy compositions.

This study aims to combine systematic ion irradiation experiments with three-dimensional atom probe (3DAP) analysis to create a database of CrRP-related quantities as a function of alloy composition and dose rate and quantitatively assess the factors influencing CrRP formation in Fe–Cr–Al alloys under irradiation. CrRP formation in Fe–Cr–Al alloys under irradiation is influenced by the incident ion species, incident energy, dose rate, irradiation dose, Cr, Al compositions, and temperature [8, 11–13]. However, these conditions vary widely from one researcher to another, making it challenging to compare their results. Furthermore, CrRP formation behavior results from a complex superposition of these various factors, and it is challenging to evaluate the influence of each factor quantitatively. Therefore, in this study, 14 Fe–Cr–Al alloys with systematically varying Cr and Al compositions were ion irradiated at three dose rates, and 3DAP analysis of the CrRPs formed were analyzed using multiple regression analysis to extract and quantify the primary factors and their interactions affecting CrRP formation. Furthermore, using data from previous studies, the behavioral changes in CrRP-related quantities over a wide range of dose rates from ion to neutron irradiation was systematically visualized, and the effects of Cr, Al composition, and dose rate were discussed. These results provide a better understanding of the CrRP formation behavior in Fe–Cr–Al alloys under irradiation and essential information for developing mechanistic models and model validation.

The paper is organized as follows. Section 2.1 describes the reasons for selecting the 14 Fe–Cr–Al alloys and describes the sample preparation methods. In Section 2.2, the ion irradiation conditions are set up, and in

Section 2.3, the 3DAP analysis procedure is described. Section 3.1 presents the 2D mapping of the 3DAP images of the CrRPs for each alloy composition and dose rate. In Section 3.2, a clustering analysis was performed on these CrRPs to quantitatively assess the CrRP-related quantities (number density, radius, volume fraction, and Cr concentration in the CrRP), organized by variables (Cr and Al compositions and dose rates). Then, Section 4.1 discusses the correlation matrix between each variable and CrRP-related quantities and extracts trends in the correlations. Section 4.2 quantifies the influence of each variable and their interaction terms on CrRP volume fraction values using multiple regression analysis. Section 4.3 demonstrates the usefulness of organizing dose and irradiation time dependence as a methodology for identifying trends in the formation behavior of CrRP-related quantities over a wide range of dose rates, from ion to neutron irradiation. Finally, the primary conclusions are summarized.

2. Experimental

2.1. Material

In this study, 14 Fe–Cr–Al alloys with systematically varied Cr and Al compositions were prepared by arc melting to clarify the formation behavior of CrRPs under ion irradiation. The 14 alloy compositions were chosen based on the range of Al compositions covering the hardness increase/suppression reported in previous thermal aging experiments [5] and the compositions for which data are available on CrRP formation under neutron irradiation [6, 13–23]. Figure 1 shows the relationship between the selected alloy compositions and the neutron irradiation data from previous studies.

To obtain the recrystallized state of pure ferrite, they were solution-annealed at 1200°C for 2 h and then quenched in water to prevent precipitation of Cr atoms during cooling. The plates were cut into $6 \times 3 \times 18$ mm square bars, and the surface of the sample on the side to be irradiated was mechanically polished and then finished with 0.3 μm colloidal silica. The samples were then cut to 0.5 mm thickness and further electropolished in a 2:8 mixture of sulfuric acid and methanol at approximately -25°C. The average grain size of the resulting samples was approximately 500 μm for all alloy types.

2.2. Ion irradiation

Fourteen Fe–Cr–Al alloy samples were loaded in the same sample holder (upper inset of Fig. 1) and simultaneously irradiated with 10.5 MeV Fe^{3+} self-ions at 350°C using a tandem accelerator at Takasaki Ion Accelerators for Advanced Radiation Application facility of the Takasaki Advanced Radiation Research Institute in Japan. The samples were irradiated to 0.24 dpa at a depth of approximately 1 μm where 3DAP analysis was performed. Three dose rates (8×10^{-6}, 8×10^{-5}, and 8×10^{-4} dpa/s) were used to investigate the dose rate dependence, which is a critical parameter for predicting CrRP formation under neutron irradiation conditions from ion irradiation conditions. The extent of the effect of ion irradiation was investigated by selecting eight alloys with relatively high Cr or low Al compositions from the masked area of 8×10^{-5} dpa/s irradiation samples (50 min irradiation) and analyzing them by 3DAP in the same way as the irradiated materials.

The ion irradiation was performed with a rastered beam at a uniformly adjusted beam current using the scanner function. The temperature of the samples was measured using thermocouples and an infrared camera, and the sample temperature during irradiation was 350°C ± 10°C, considering beam heating. The irradiation conditions of Fe ions in this study were determined with reference to Zhao et al. [8]. The damage and ion stopping depth profiles in Fe–Cr–Al alloys irradiated with 10.5 MeV Fe^{3+} ions were calculated with the SRIM code [24]. Following the calculation method proposed by Stoller et al. [25] which is widely accepted as the standard for dpa reporting, the calculations were performed using the "quick Kinchin–Pease calculation" option, selecting the recommended displacement threshold energy of 40 eV [26] for iron or iron-based alloys. The damage energy was then calculated according to Eq. (5b) in [25], and the obtained damage energy was used to calculate the number of displacements according to Eq. (1) in [25]. To determine the extent to which the damage profiles differ among the 14 alloys used in this study, a comparison of pure iron and two alloys with very different alloy compositions (Fe–40Cr and Fe–15Cr–8Al (at.%)) is shown in Fig. 2. Although there are some differences in the profiles near the peaks of damage and Fe ion implantation, there is little difference at approximately 1 μm, so the damage dose is assumed here to be 0.24 dpa for all alloys. In the post-irradiation 3DAP analysis, the intermediate region (a depth of approximately 1 μm) was selected as the analysis region to minimize surface effects and the influence of irradiation-introduced Fe ions, as in Zhao et al. [8].

2.3. 3DAP characterization

Samples for 3DAP analysis were prepared using a standard lift-out technique and a focused ion beam. The CrRPs produced under ion irradiation were analyzed using 3DAP (LEAP 5000XS, CAMECA). The 3DAP analyses were performed in laser mode with a laser pulse energy of 30 pJ at a base temperature of 30 K. The acquired data were reconstructed using CAMECA IVAS 3.8.16 software. To correctly deconvolve the overlapping peaks at mass-to-charge ratios of 27 Da ($^{27}Al^{+}$, $^{54}Cr^{2+}$, $^{54}Fe^{2+}$) and 54 Da ($^{54}Cr^{+}$, $^{54}Fe^{+}$), both peaks were first assigned to Fe, and the measured Cr and Al compositions were corrected based on the natural isotopic abundance of each element [6, 27]. This treatment significantly improved the deviation of the Al content in the matrix from the nominal value, whereas the Cr content in the matrix composition was largely unaffected. Figure 3 compares the Al matrix composition before and after correction and the nominal values for each alloy, and Table 1 gives the corrected alloy compositions of Cr and Al.

To streamline the linkage with various data analyses of CrRP-related quantities to be performed in Section 4, a unique clustering analysis script was created using R (version 4.3.1) and MATLAB [29] for the 3DAP analysis. The clustering analysis of Cr-rich regions was performed using the maximum separation method [18, 30]. Here, the maximum separation distance d_{max}, which defines whether Cr atoms belong to the same cluster, ranged from 0.4 to 0.6 nm, and the minimum number of Cr atoms in a statistically significant cluster N_{min} ranged from 30 to 100. The envelope and erosion method [30, 31] was used to extract Fe and Al atoms in CrRPs extracted by the maximum separation method to correctly calculate cluster size, number density, composition, and volume fraction.

The number of samples used for 3DAP analysis was 49, consisting of 41 irradiated materials (three different damage rates) and 8 thermally aged materials, one tip per condition. The 3DAP analysis volume was carefully chosen for each condition to avoid artifacts such as poles due to diffraction. The volumes and total number of atoms for each sample used in the 3DAP analysis are listed in Table 1.

Then, the CrRP number density N_{CrRP} was calculated by [8, 18]

$$N_{\mathrm{CrRP}} = \frac{n_{\mathrm{CrRP}}}{V} \simeq \frac{n_{\mathrm{CrRP}}\rho Q}{n_{\mathrm{atom}}^{\mathrm{tot}}}, \tag{1}$$

where n_{CrRP} is the number of measured CrRPs in the reconstructed volume, V is the reconstructed volume, ρ is the density of the CrRPs (assumed to be 84.3 atom nm^{-3}, the same as α-Fe), Q (= 0.80) is the detection efficiency of the atom probe used, and $n_{\mathrm{atom}}^{\mathrm{tot}}$ is the total number of atoms in the reconstructed volume. The size (radius) of CrRPs, R_{CrRP}, was calculated using the spherical equivalent radius [30] given by the following formula [8, 18]:

$$R_{\mathrm{CrRP}} = \sqrt[3]{\frac{3n_{\mathrm{atom}}^{\mathrm{CrRP}}}{4\pi\rho Q}}, \tag{2}$$

where $n_{\mathrm{atom}}^{\mathrm{CrRP}}$ is the number of atoms detected in each CrRP. The CrRP volume fraction f_{CrRP} is calculated as follows [8, 18]:

$$f_{\mathrm{CrRP}} = \frac{\sum n_{\mathrm{atom}}^{\mathrm{CrRP}}}{n_{\mathrm{atom}}^{\mathrm{tot}}}, \tag{3}$$

that is the sum of the number of atoms contained in CrRPs within the analyzed volume divided by the total number of atoms in the reconstructed volume.

3. Results

3.1. Visualization of CrRPs by 3DAP analysis

First, to give an overview of the CrRP distribution differences by 3DAP analysis of 14 Fe–Cr–Al alloys irradiated with ions at three dose rates, a planar projection of Cr atoms in an arbitrary volume of each alloy is shown in Fig. 4. As the Cr composition of the matrix increases, CrRP formation is enhanced. However, as the Al composition increases, the formation of CrRPs is suppressed. Furthermore, CrRP formation decreases as the dose rate increases. Uniform and distinct CrRPs were observed in the high Cr alloys without Al, whereas the CrRPs were obscured when adding Al. However, there appeared to be little systematic change in the cluster diameter for each variable. No CrRP formation was observed in thermally aged materials, except for Fe–21Cr. This result indicates that irradiation promotes CrRP formation. Furthermore, it is proposed that the Cr composition significantly affects CrRP formation, particularly that the formation is rapidly accelerated at high Cr additions above a specific level.

As a peculiar behavior, in Fe–10Cr, CrRP formation was only observed at the highest dose rates of 8 × 10^{-4} dpa/s. This result contrasts with other alloys where CrRP formation is suppressed at higher dose rates. The microstructure was observed after etching the alloy surfaces to investigate the cause. It was found that, in some cases, martensitic transformation occurred in Fe–10Cr during rapid cooling after solution annealing. In such a mixed ferrite/martensite microstructure, the formation behavior of CrRPs might differ from that in the ferrite phase. On the other hand, studies have shown that the mechanism of CrRP formation during thermal aging is spinodal decomposition in Fe–40Cr [32]. This mechanism differs from the nucleation-type mechanism for alloys other than Fe–40Cr used in this study. In this study, a modulated structure with many interconnected Cr-rich regions, characteristic of spinodal decomposition, was observed even under ion irradiation (Fig. 4). Therefore, the number density and size of isolated Cr-rich clusters could not be determined. Therefore, the mechanism of CrRP formation under ion irradiation in Fe–10Cr with mixed ferrite/martensite microstructures and in Fe–40Cr undergoing spinodal decomposition will be discussed in a future paper and will not be included in the multiple regression model developed in Section 4.2.

3.2. Quantification of CrRP-related quantities by clustering analysis

The clustering analysis described in Section 2.3 was used to identify the Cr-rich regions in each Fe–Cr–Al alloy shown in Fig. 4 and extracted as individual clusters for quantitative analysis. Table 1 summarizes the obtained quantities: (a) CrRP number density, N_{CrRP}, (b) CrRP radius, R_{CrRP}, (c) CrRP volume fraction, f_{CrRP}, and (d) Cr concentration in CrRPs, $C_{\mathrm{Cr}}^{\mathrm{CrRP}}$, and they are shown in Figs. 5 (a)–(d) against each variable (Cr and Al matrix compositions and dose rates). Each figure also shows data for Fe–18Cr from Zhao et al. [8] obtained under almost the same irradiation conditions as in this study. Comparing both data in each figure, the values of all CrRP measurements are comparable. Figure 5 (a) shows that the CrRP number density increases with higher matrix Cr composition, lower matrix Al composition, and lower dose rate. However, for the CrRP radius in Fig. 5 (b), the dependence on each variable is less clear, although there is a tendency for the radius to decrease slightly with increasing Cr composition. The size in Fe–12Cr is larger than the others. The dependence on each variable in the CrRP volume fraction (Fig. 5 (c)) and the Cr composition in CrRPs (Fig. 5 (d)) show similar trends to those in the CrRP number density (Fig. 5 (a)). The gray points in Figs. 5 (a)–(d) correspond to alloy compositions where the CrRPs did not form or was below the detection limit of the APT analytical volumes used here and can, therefore, be considered to represent the rough critical compositional conditions for CrRP formation under the irradiation conditions in this study.

4. Discussion

4.1. Correlation analysis of CrRP-related quantities

To further clarify the quantitative relationship between these CrRP-related quantities and each variable, Fig. 6 shows the correlation matrix. The label in the upper left corner of each panel shows the Spearman's correlation coefficient ρ between the two corresponding variables for all dose rate data in each panel, along with significance level symbols * based on the p-value calculated from the correlation test (a higher number of * indicates a higher significance level).

For the CrRP number density, a positive correlation with the Cr matrix composition ($\rho = 0.54^{**}$) and a weak negative correlation trend with the Al matrix composition ($\rho = -0.34$) were observed. Simultaneously, the CrRP number density increased with lower dose rates. The CrRP radius showed a weak but non-significant negative correlation with Cr and Al matrix compositions ($\rho = -0.24$ and $\rho = -0.28$, respectively). No clear correlation with dose rate was observed.

The Cr concentration in CrRPs tends to decrease with increasing CrRP radius ($\rho = -0.3$). This trend may reflect the unusually large CrRP radius data observed in Fe–12Cr, where fewer CrRPs are formed. The shape of the CrRPs in Fe–12Cr was somewhat flat rather than spherical as observed in all the other alloys. The cause of this is unknown at this time and is being investigated in conjunction with TEM observations. The correlations between the CrRP volume fraction and Cr composition (and Al composition) and between the Cr concentration in the CrRP and Cr composition (and Al composition) showed similar trend to the correlations between the CrRP number density and these variables. A strong correlation ($\rho \geq 0.8^{***}$) was found between the three measurements of CrRP number density, volume fraction, and Cr concentration. The Cr concentration in the CrRPs is higher at lower dose rates, indicating that the CrRP formation state is more advanced at lower dose rates. However, to clarify this, comparisons at the same irradiation dose and according to irradiation time are needed.

4.2. Multiple regression model to assess the effect of each variable and their interactions on CrRP volume fraction

Among the three CrRP-related quantities (number density, volume fraction, and Cr concentration) for which strong positive correlations were identified in the previous section, the CrRP volume fraction, which is strongly related to embrittlement, is selected as representative, and the effect of each variable (explanatory variable) on the CrRP volume fraction (objective variable) is quantitatively assessed by multiple regression analysis.

Although systematic experimental data covering various Cr and Al compositions were available for this study, the limited number of data (sample size) for regression modeling led to selecting a linear multiple regression model with a low risk of overfitting and robustness to extrapolation rather than a complex nonlinear model with a high risk of overfitting. Linear here means that the model is linear regarding the coefficients of each explanatory variable. To account for the possibility that the response of the objective variable might not be independent for each explanatory variable, the three explanatory variables (Cr, Al matrix compositions, and dose rate) were considered as primary effects and the combination of all multiplications of these explanatory variables as interaction terms. Then, the multiple regression model is given by

$$y_i = \beta_0+\beta_1 x_{i1}+\beta_2 x_{i2}+\beta_3 x_{i3}+\beta_{12} x_{i1} x_{i2}+\beta_{23} x_{i2} x_{i3}+\beta_{31} x_{i3} x_{i1}+\beta_{123} x_{i1} x_{i2} x_{i3}+\epsilon_i, \quad (4)$$

where y_i is the i-th record (sample) of the objective variable (CrRP volume fraction), x_{i1}, x_{i2}, and x_{i3} are the i-th records of the Cr matrix composition, Al matrix composition, and dose rate, respectively, and $x_{i1}x_{i2}$, $x_{i2}x_{i3}$, $x_{i3}x_{i1}$, and $x_{i1}x_{i2}x_{i3}$ are the possible interaction terms. The coefficient β for each term is the regression coefficient and is determined by training. ϵ_i in the last term on the right-hand side of Eq. (4) is the error term, assuming a normal distribution. As a preprocessing step, the dose rate was log-transformed because it has an extensive range of two orders of magnitude compared to the other primary effects. All variables were standardized to correctly account for interaction effects. The cases of Fe–10Cr, which might contain martensitic phases in some samples, and Fe–40Cr, with a spinodal decomposition mechanism, were excluded from the model training data.

In general, adding explanatory variables to a regression model improves the goodness-of-fit to the training data but is likely to lead to overfitting that reduces predictive performance. One of the most popular model selection theories that address this goodness-of-fit/reliability trade-off is Akaike's Information Criteria (AIC) [33], comprising a goodness-of-fit term and an increasing parameter penalty term. A multiple regression model was constructed to minimize the AIC by starting with the full model and using a backward selection method where explanatory variables that increase the AIC are removed. The variance inflation factor (VIF), a measure of the stability of the multiple regression models generated, is less than 1.3 for all explanatory variables, indicating no multicollinearity in the models. Furthermore, various regression diagnostics on the validity of the linear model assumptions showed that the normality, global statistics, skewness, kurtosis, link function, and heteroscedasticity of the predicted data were all within acceptable limits ($p > 0.07$), ensuring the validity of the model.

Fig. 7 (a) shows the prediction performance of the model on the experimental data. The generated model showed a very good fit, with a degree of freedom adjusted $R^2_{\mathrm{adj}} = 0.89$ ($p < 10^{-12}$: highly significant). Figure 7 (b) is a forest plot of the coefficient estimates and significance level magnitudes for the seven explanatory variables (three primary effects and four interactions) selected by the AIC minimum condition. The positive and negative values represent the contribution to an increase or decrease in the objective variable (CrRP volume fraction), respectively, with absolute values indicating the magnitude of the contribution. The magnitude of the contribution to the CrRP volume fraction by each of the primary effects that showed a significant correlation with the CrRP volume fraction, as shown in Fig. 6, were the Cr matrix composition ($+0.48^{***}$), Al matrix composition (-0.34^{***}), and dose rate (-0.35^{***}). In addition to the primary effects, several significant interaction terms occurred, indicating that complex elementary processes are involved in the formation behavior of CrRPs. Particularly important interactions were between the dose rate and the Cr matrix composition, and between the Cr and Al matrix compositions. The interaction terms involving all three primary effects were significant, but as this interpretation is challenging, the more detailed contribution of the interaction terms between the two variables was analysed.

Here, the effects of the interactions between the explanatory variables were assessed using the individual conditional expectations (ICE) plot shown in Fig. 7 (c). The ICE visualizes in a single line how the predicted values for each piece of data change when the explanatory variables are changed. Thus, if there are interactions between the explanatory variables, it is possible to observe the heterogeneous relationship of the predicted values resulting from these interactions. The left plot in Fig. 7 (c) shows that for all data, the CrRP volume fraction increases with increasing Cr composition, as indicated by the gray lines. However, the CrRP volume fraction hardly changes with increasing Cr composition when the Al composition is greater than 12 at.%, as indicated by the red lines. The middle and right plots in Fig. 7 (c) show the dependence of the CrRP volume fraction on the Al composition and dose rate, respectively. These figures show that the CrRP volume fraction decreases with increasing Al composition and dose rate in both cases (gray lines). However, when the Cr composition is less than 13 at.%, the CrRP volume fraction remains low even at lower Al compositions and dose rates (red lines). The results indicate a clear interaction between the explanatory variables, indicating that reducing the Cr composition and increasing the Al composition contribute to the suppression of CrRP formation even under low dose rate neutron irradiation, and further research is required.

Next, in Fig. 7 (d), the predicted contours from the multiple regression model are plotted on the Al and Cr composition dependence map of the CrRP volume fraction data obtained in this study. The predicted contours are drawn based on the estimated values at each grid point of the 100×100 partition of the Cr and Al composition ranges in the figure. The predicted contours show an increasing CrRP volume fraction with the increasing Cr matrix composition and decreasing Al matrix composition and dose rate. It is of engineering importance to visualize the critical conditions for CrRP formation that can be read from these contours.

The machine learning modeling of the CrRP volume fraction based on ion irradiation experiments performed in this study could construct an accurate model in the linear multiple regression models because the mathematical functions of the model were expressive enough to capture the complexity of the problem. However, caution should be exercised when predicting neutron irradiation conditions with dose rates 1–2 orders of magnitude lower than the minimum dose rate of 8×10^{-6} dpa/s considered in this study. The reason is that it is unlikely that CrRP-related quantities will continue to increase with decreasing dose rates. Therefore, compared at the same dose, below a specific dose rate, the increase rate of CrRP-related quantities should slow down (or even start to decrease) due to nonlinear effects. Here, mathematically expressive nonlinear models that can capture beneficial patterns should be considered. However, more complex regression models involving nonlinear effects require sufficient training data to avoid overfitting the model. Therefore, in addition to the CrRP data up to the 0.24

dpa obtained in this study, ion irradiation data should be extended to higher damage levels. This would help discuss the damage level dependence, an essential variable in CrRP formation behavior under irradiation. Therefore, additional ion irradiation experiments comparable to high damage levels (e.g., 0.8 and 1.8 dpa), for which neutron irradiation data are relatively abundant, are currently being performed in this study.

However, to predict the formation behavior of CrRPs under neutron irradiation using ion irradiation experiments, developing a mechanistic physical model that can reasonably relate to the dose rate gap is essential. Therefore, we are developing a mechanistic physical model based on the phase-field method. The quantitative knowledge of the influence and interaction of each variable on various physical quantities related to CrRPs, obtained by the multiple regression model developed in this study, should provide critical information for developing mechanistic physical models and play an essential role in verifying computational results.

4.3. Prospects for predicting neutron irradiation conditions with the addition of data from previous studies

So far, a detailed discussion of the CrRP-related quantities obtained from the ion irradiation experiments conducted in this study has been presented. However, the final objective is to predict the CrRP formation behavior under neutron irradiation conditions based on the results obtained under ion irradiation conditions. Therefore, it is necessary to accumulate knowledge of the production behavior of CrRP-related quantities over a wide range of dose rates. This section provides an overview of the effect of dose rate on the production behavior of CrRP-related quantities over a wide range of dose rates based on data obtained in previous studies, and discusses the results to guide future research.

Comparisons based on irradiation doses are commonly used to investigate the effect of dose rate. However, as shown in thermal aging experiments, the formation behavior of CrRPs depends on the thermal aging time. It is critical to consider the effect of irradiation time during irradiation. Although the irradiation time required to achieve the same dose is inversely proportional to the dose rate, the dose and irradiation time-dependent visualization of CrRP formation behavior should provide valuable information for understanding the effect of dose rate on CrRP formation behavior. Therefore, Fig. 8 shows the dose dependence (left panel) and irradiation time dependence (right panel) of (a) CrRP number density, (b) radius, (c) volume fraction, and (d) Cr concentration. For the irradiation dose dependence, data from previous ion [8, 11–13] and neutron [6, 7, 17, 19, 21–23] irradiation studies were used with the present data. For the irradiation time dependence, data from thermal aging studies [7, 8, 27, 34–38] were also used as a limit for the zero dose rate.

First, the irradiation dose dependence of the left panel of Fig. 8 is examined. All thermal aging data are not shown because the irradiation dose dependence is not seen due to zero damage. These figures show that all measured quantities (a)–(d) rapidly increase up to low irradiation doses, such as 0.3–0.5 dpa, after which the increase slows down. For the CrRP number density in (a), unlike the other measured quantities, a peak is reached at a specific irradiation dose and then begins to decrease. This result indicates that above a specific number density, the distance between the CrRPs decreases and some phases combine. This CrRP number density decreases uniformly with increasing Al additions. However, in (b)–(d), the CrRP-related quantities maintain a gradual increasing trend with irradiation dose. In the dose rate region corresponding to ion irradiation, these CrRP-related quantities decrease with increasing Al addition, as shown in this study. However, in the dose rate range corresponding to neutron irradiation, the tendency for the formation of these CrRPs to be suppressed by Al addition cannot be easily confirmed. This result might be due to the lack of neutron irradiation data, making it challenging to determine the degree of influence of each variable.

For the Al-free Fe–Cr alloys, the ion and neutron irradiation data have several plot points in the same irradiation dose range. Although the uncertainty is large due to the small number of data points, considering the size of the points representing the Cr composition, these data points are on a constant trend line regardless of the dose rate. However, the results of the ion irradiation experiments in this study show that at a dose of 0.24 dpa, the CrRP-related quantities are higher at lower dose rates. At the dose of 10 dpa, phase-field calculations by Ke et al. [10] reported that the CrRP-related quantities do not depend much on the dose rate and little CrRP is formed above 10^{-5} dpa/s. Zhao et al. [8] highlighted that in the CrRP definition by Ke et al. [10], the Cr concentration is higher than 75–80 at.%, so it is possible that CrRPs at low Cr concentrations, such as those obtained in this experimental study, were not detected. This result might have contributed to the discrepancy with the present experimental results, where a clear dose rate dependence was observed. However, in addition to the difference in irradiation dose between the calculation and the present experiment, the dose dependence of CrRP formation behavior might also be based on a complex process that depends on Cr composition, Al composition, and their combination. Therefore, further studies are needed to clarify the dose dependence of CrRP-related quantities when compared at the same damage level. A critical experimental problem is that neutron irradiation data with low dose rates tend to have higher doses, and the range of doses that can be directly compared with ion irradiation data is narrow. Therefore, it is essential to extend the range of high damage dose data from ion irradiation with different dose rates to better understand the CrRP formation behavior under neutron irradiation.

The irradiation time dependence is examined in the right column of Fig. 8. The respective CrRP-related quantities in (a)–(d) are organized by smoother and more continuous trend lines than the irradiation dose dependence shown in the respective figures in the left column. The CrRP number density in (a) went from increasing to decreasing at 10–100 h. Relatedly, the CrRP radius in (b) increases at 10–100 h. The other two, (c) CrRP volume fraction and (d) Cr concentration in CrRPs, show similar continuous increasing behavior with irradiation time. Regarding the irradiation (thermal aging) time, no overlap occurs between the ion irradiation and thermal aging data, but an overlap occurs between the neutron irradiation and thermal aging data. Although the dose rate of neutron irradiation is low, it is naturally affected by irradiation. Therefore, to understand the CrRP formation behavior, the superposition effect of the CrRP formation mechanism during thermal aging and the CrRP formation mechanism during irradiation must be considered. Furthermore, the neutron irradiation and thermal aging data differ in the temperature range of 300°C–390°C and 475°C–500°C respectively. Despite these seemingly substantial differences, the irradiation time dependence of the respective CrRP-related quantities in (a)–(d) shows a similar trend for the neutron irradiation and thermal aging data. This result does not mean that the effect of irradiation can be ignored, but indicates that the degree of influence of irradiation (thermal aging) time on CrRP formation behavior is relatively large. To clarify this point, futher understanding of the influence of temperature under irradiation is required. Nevertheless, the results could have valuable implications for constructing and validating predictive models of CrRP formation. In this context, an essential feature of a suitable predictive model is that, in addition to being able to correctly describe the effect of dose rate, it must have the generality to explain the CrRP formation behavior due to thermal aging as an extreme limit with zero dose rate.

In this study, CrRP-related quantities were measured at the same irradiation dose at three dose rates. As the irradiation time is inversely proportional to the dose rate at the same irradiation dose, the assessment of the irradiation time dependence and the dose rate dependence are practically indistinguishable regarding the data of this study. Therefore, to clarify the influence of dose rate also in terms of irradiation time dependence, it is necessary to obtain and compare data at different dose rates and times by extending the data at higher irradiation doses in addition to the data at a dose of 0.24 dpa obtained in this study. Additional ion irradiation experiments for this purpose are in progress.

5. Summary

For Fe–Cr–Al (ODS) alloys to be developed as ATF cladding for light water reactors, the challenge is to accurately predict the formation of CrRPs that occur at relatively low irradiation temperatures and cause embrittlement. However, CrRP formation under neutron irradiation is poorly understood due to the global limitations of irradiated reactors. Therefore, this study used ion irradiation as an alternative to neutron irradiation, and CrRPs formed at three irradiation dose rates were systematically quantified for 14 Fe–Cr–Al model alloys by 3DAP analysis, yielding the following results.

- Correlations between each variable
  - CrRP number density, volume fraction, and Cr concentration showed a strong correlation with Cr composition and a negative correlation with Al composition and dose rate.
  - CrRP radius showed a weak negative correlation trend (no significant difference) with Cr and Al compositions, but no correlation with dose rate.
  - Strong bivariate correlations were observed between the measured CrRP number density, volume fraction and Cr concentration in CrRPs.
- Synergistic effects of variables on CrRP volume fraction by multiple regression analysis

  - The higher the Al composition, the lower the increase in CrRP volume fraction with increasing Cr composition.
  - The lower the Cr composition, the smaller the increase in CrRP volume fraction with decreasing Al composition and dose rate.

- Database analysis to estimate CrRP formation behavior over the damage rate range from ion irradiation to neutron irradiation

  - Regarding dose dependence, all CrRP-related quantities increase rapidly up to low doses of 0.3–0.5 dpa, after which the changes become slower.
  - For irradiation time dependence, the data for each CrRP-related quantity show a smooth and continuous trend with irradiation time when the thermal aging data, where the dose rate is assumed to be zero, are considered, and the trend is similar for the neutron irradiation and thermal aging data.

In summary, the database of CrRP-related quantities obtained in this study is valuable for validating and improving various mechanistic prediction models for CrRP formation behavior under neutron irradiation. However, due to the paucity of data corresponding to higher irradiation doses at different dose rates, further irradiation data are needed to clarify the effects of the dose rates identified in this study, and experiments are underway. Once this is achieved, complementary methodologies based on data-driven models and advances in mechanistic numerical prediction models will pave the way for predicting the production behavior of CrRPs under neutron irradiation conditions.

Acknowledgments

This work was supported in part by JSPS KAKENHI Grant Number 22H02013, and performed under the Shared Use Program of QST Facilities. We are grateful to Mr Fujita and Mr Otomo of NIHON AXIS Co., Ltd. for their technical support in the preparation of the samples used in the ion irradiation experiments.

References

[1] S. Ukai, K. Sakamoto, S. Ohtsuka, S. Yamashita, A. Kimura, Review: Alloy design and characterization of a recrystallized FeCrAl-ODS cladding for accident-tolerant BWR fuels: An overview of research activity in Japan, J. Nucl. Mater. 583 (2023) 154508.

[2] R.M. Fisher, E.J. Dulis, K.G. Carroll, Identification of the precipitate accompanying 885-Degrees-F embrittlement in chromium steels. Trans. Am. Inst. Min. Metall. Pet. Eng. 197 (1953) 690-–695.

[3] R. Lagneborg, Deformation in an iron–30% chromium alloy aged at 475°C, Acta Mater. 15 (1967) 1737–1745.

[4] P.J. Grobner, The 885°F (475°C) embrittlement of ferritic stainless steels, Met. Trans. 4 (1973) 251–260.

[5] S. Kobayashi, T. Takasugi, Mapping of 475°C embrittlement in ferritic Fe–Cr–Al alloys, Scr. Mater. 63 (11) (2010) 1104–1107.

[6] S.A. Briggs, P.D. Edmondson, K.C. Littrell, Y. Yamamoto, R.H. Howard, C.R. Daily, K.A.Terrani, K. Sridharan, K.G. Field, A combined APT and SANS investigation of α' phase precipitation in neutron-irradiated model FeCrAl alloys, Acta Mater. volume 129 (2017) 217–228.

[7] E.R. Reese, N. Almirall, T. Yamamoto, S. Tumey, G.R. Odette, E.A. Marquis, Dose rate dependence of Cr precipitation in an ion-irradiated Fe–18Cr alloy, Scr. Mater. 146 (2018) 213–-217 .

[8] Y. Zhao, A. Bhattacharya, C. Pareige, C. Massey, P. Zhu, J.D. Poplawsky, J. Henry, S.J. Zinkle, Effect of heavy ion irradiation dose rate and temperature on α' precipitation in high purity Fe–18%Cr alloy, Acta. Mater. 231 (2022) 117888.

[9] K.N. Thomas, G.S. Was, J. Nucl.Effect of cascade size and damage rate on α' precipitate stability in Fe–15Cr, J. Nucl. Mater. 585 (2023) 154615.

[10] J.-H. Ke, E.R. Reese, E.A. Marquis, G.R. Odette, D. Morgan, Flux effects in precipitation under irradiation e Simulation of Fe–Cr alloys, Acta Mater. 164 (2019) 586–601.

[11] O. Tissot, C. Pareige, E. Meslin, B. Décamps, J. Henry, Influence of injected interstitials on α' precipitation in Fe–-Cr alloys under self-ion irradiation, Mater. Res. Lett. 5 (2016) 117–123.

[12] P. Zhu, Y. Zhao, Y.-R. Lin, J. Henry, S.J. Zinkle, Defect-specific strength factors and superposition model for predicting strengthening of ion irradiated Fe18Cr alloy, J. Nucl. Mater. 588 (2024) 154823.

[13] E. Marquis, B. Wirth, G. Was, Characterization and Modeling of Grain Boundary Chemistry Evolution in Ferritic Steels under Irradiation, Univ. of Michigan, Ann Arbor, MI (United States), 2016.

[14] M. Miller, R. Stoller, K. Russell, Effect of neutron-irradiation on the spinodal decomposition of Fe–32%Cr model alloy, J. Nucl. Mater. 230 (1996) 219–225.

[15] F. Bergner, A. Ulbricht, C. Heintze, Estimation of the solubility limit of Cr in Fe at 300°C from small-angle neutron scattering in neutron-irradiated Fe–Cr alloys, Scr. Mater. 61 (2009) 1060–1063 .

[16] C. Heintze, F. Bergner, A. Ulbricht, H. Eckerlebe, The microstructure of neutron-irradiated Fe–Cr alloys: a small-angle neutron scattering study, J. Nucl. Mater. 409 (2011) 106–111.

[17] V. Kuksenko, C. Pareige, P. Pareige, Cr precipitation in neutron irradiated industrial purity Fe–Cr model alloys, J. Nucl. Mater. 432 (2013) 160–165.

[18] M. Bachhav, G. Robert Odette, E.A. Marquis, α' precipitation in neutron-irradiated Fe–Cr alloys, Scr. Mater. 74 (2014) 48–51.

[19] W.-.Y. Chen, Y. Miao, Y. Wu, C.A. Tomchik, K. Mo, J. Gan, M.A. Okuniewski, S.A. Maloy, J.F. Stubbins, Atom probe study of irradiation-enhanced α' precipitation in neutron-irradiated Fe–Cr model alloys, J. Nucl. Mater. 462 (2015) 242–249.

[20] K.G. Field, X. Hu, K.C. Littrell, Y. Yamamoto, L.L. Snead, Radiation tolerance of neutron-irradiated model Fe–Cr–Al alloys, J. Nucl. Mater. 465 (2015) 746–755.

[21] C.P. Massey, D. Zhang, S.A. Briggs, P.D. Edmondson, Y. Yamamoto, M.N. Gussev, K.G. Field, Deconvoluting the Effect of Chromium and Aluminum on the Radiation Response of Wrought FeCrAl Alloys After Low-Dose Neutron Irradiation, J. Nucl. Mater. 549 (2021) 152804.

[22] P.D. Edmondson, S.A. Briggs, Y. Yamamoto, R.H. Howard, K. Sridharan, K.A. Terrani, K.G. Field, Irradiation-enhanced α' precipitation in model FeCrAl alloys, Scr. Mater. 116 (2016) 112–116.

[23] D. Zhang, S.A. Briggs, P.D. Edmondson, M.N. Gussev, R.H. Howard, K.G. Field, Influence of welding and neutron irradiation on dislocation loop formation and α' precipitation in a FeCrAl alloy, J. Nucl. Mater. 527 (2019) 151784.

[24] J.F. Ziegler, J.P. Biersack, M.D. Ziegler, SRIM—The Stopping and Range of Ions in Matter (SRIM Co., Chester, 2008); www.srim.org

[25] R.E. Stoller, M.B. Toloczko, G.S. Was, A.G. Certain, S. Dwaraknath, F.A. Garner, On the use of SRIM for computing radiation damage exposure, Nucl. Instrum. Methods Phys. Res. B 310 (2013) 75–80.

[26] ASTM E521, Standard Practice for Neutron Radiation Damage Simulation by Charged-Particle Irradiation, Annual Book of ASTM Standards, Vol. 12.02, ASTM International, West Conshohocken, PA, 2009.

[27] Z. Yang, Z.X. Wang, C.H. Xia, et al. Aluminum suppression of α' precipitate in model Fe–-Cr–-Al alloys during long-term aging at 475°C, Materials Science and Engineering A 772 (2020) 138714.

[28] A. Cerezo and L. Davin, Aspects of the observation of clusters in the 3-dimensional atom probe, Surface and Interface Analysis, 353, (2007) 184–188.

[29] MATLAB. (2020). 9.9.0.1524771 (R2022b). Natick, Massachusetts: The MathWorks Inc.

[30] L.T. Stephenson, M.P. Moody, P.V. Liddicoat, S.P. Ringer, New techniques for the analysis of fine-scaled clustering phenomena within atom probe tomography (APT) data, Microsc. Microanal. 13 (06) (2007) 448–463.

[31] D. Vaumousse, A. Cerezo, P.J. Warren, A procedure for quantification of precipitate microstructures from three-dimensional atom probe data, Ultramicroscopy 95 (2003) 215–221.

[32] M.K. Miller, J.M. Hyde, M.G. Hetherington, A. Cerezo, G.D.W. Smith, C.M. Elliott, Spinodal decomposition in Fe–Cr alloys: Experimental study at the atomic level and comparison with computer models—I. Introduction and methodology, Acta metall. mater. 43 (1995) 3385–3401.

[33] H. Akaike, Information theory and an extension of the maximum likelihood principle, Proceedings of the 2nd International Symposium on Information Theory, Petrov, B. N., and Caski, F. (eds.), Akadimiai Kiado, Budapest: 267–281 (1973).

[34] O.A. Korchuganova, M. Thuvander, A.A. Aleev, S.V. Rogozhkin, T. Boll, T. V. Kulevoy, Microstructural evolution of Fe–22%Cr model alloy under thermal ageing and ion irradiation conditions studied by atom probe tomography, J. Nucl. Mater. 477 (2016) 172–177.

[35] S.V. Rogozhkin, O.A. Korchuganova, A.A. Aleev, Kinetics of α' phase nucleation under thermal ageing of Fe–22% Cr alloy, Inorg. Mater. Appl. Res. 2 (2016) 210–213.

[36] S. Novy, P. Pareige, C. Pareige, Atomic scale analysis and phase separation understanding in a thermally aged Fe–20 at.%Cr alloy, J. Nucl. Mater. 384 (2009) 96–102.

[37] P. Zhu, Y. Zhao, S. Agarwal, J. Henry, S.J. Zinkle, Toward accurate evaluation of bulk hardness from nanoindentation testing at low indent depths, Mater. Des. 213 (2022) 110317.

[38] M. Arivu, A. Hoffman, H. Wen, J. Poplawsky, Understanding the influence of grain size on α' Cr precipitation in Fe–21Cr–5Al alloy during thermal aging using atom probe tomography, Microsc. Microanal. 27 (2021) 3380–3382.

Table 1: List of Fe–Cr–Al alloy compositions used in the study and the different CrRP measurements obtained from the 3DAP analysis. One tip per condition was analyzed and the volume used for 3DAP analysis is expressed as $L_x \times L_y \times L_z$ (nm) and the number of atoms in the volume is denoted by N_{tot}. The symbol "–" indicates that it was not observed. The numbers in brackets indicate standard deviations, values obtained from the data distribution for measurements other than the CrRP number density, and values obtained from the Poisson probability distribution proposed by Cerezo et al. [28] for CrRP number density. For readability, each alloy composition is shown without the notation "Fe–", which is common to all.

No.		**compn. (SEM/EDS)**		**compn. (3DAP)**		**Dimensions used for 3DAP analysis**				**Results of 3DAP analysis**			
	Alloy	Cr (at.%)	Al (at.%)	Cr (at.%)	Al (at.%)	L_x (nm)	L_y (nm)	L_z (nm)	N_{tot} (10^6 atoms)	N_{CrRP} (10^{23} m^{-3})	R_{CrRP} (nm)	f_{CrRP} (vol.%)	$C_{\mathrm{Cr}}^{\mathrm{CrRP}}$ (at.%)
8×10^{-6} **dpa/s**													
1	10Cr	10.7	0.0	–	–	–	–	–	–	–	–	–	–
2	10Cr-5Al	10.2	8.9	11.7	10.3	15	15	60	0.87	–	–	0.0	–
3	12Cr	12.9	0.0	12.2	0.4	20	30	140	5.81	0.1 (0.0)	1.5 (0.6)	0.7	29 (4)
4	12Cr-4.5Al	12.2	8.0	11.5	9.0	20	10	240	3.46	9.4 (1.4)	1.0 (0.1)	0.4	34 (5)
5	12Cr-6Al	12.2	10.6	10.7	11.9	20	10	220	3.63	18.0 (2.0)	0.7 (0.1)	0.4	30 (4)
6	15Cr	16.0	0.0	14.4	0.7	20	20	180	4.81	58.0 (2.8)	0.8 (0.3)	2.0	36 (6)
7	15Cr-4Al	15.4	6.6	13.9	9.6	20	15	290	5.09	45.0 (2.1)	1.0 (0.3)	1.7	40 (7)
8	15Cr-8Al	14.7	14.2	13.6	15.5	30	15	180	6.24	27.0 (1.8)	1.1 (0.2)	1.5	29 (3)
9	17.5Cr	18.2	0.0	17.6	0.1	15	15	140	2.15	62.0 (4.4)	1.0 (0.3)	3.1	48 (6)
10	17.5Cr-3Al	17.9	5.7	16.4	6.8	20	5	200	1.55	110.0 (7.5)	0.7 (0.1)	1.9	43 (6)
11	17.5Cr-8Al	17.0	14.3	9.7	13.9	20	5	200	1.07	–	–	0.0	–
12	21Cr	21.8	0.0	19.3	0.3	30	10	100	1.94	95.0 (5.6)	1.1 (0.2)	6.0	58 (5)
13	21Cr-8Al	20.2	14.2	19.1	15.5	35	20	100	4.63	17.0 (1.6)	0.9 (0.1)	0.5	42 (4)
14	40Cr	38.8	0.0	36.1	0.6	–	–	–	–	–	–	–	–
8×10^{-5} **dpa/s**													
15	10Cr	10.7	0.0	10.2	0.1	–	–	–	–	–	–	0.0	–
16	10Cr-5Al	10.2	8.9	9.8	9.4	10	30	150	3.96	–	–	0.0	–
17	12Cr	12.9	0.0	11.6	0.3	30	30	60	4.63	2.2 (0.6)	2.0 (0.3)	0.8	27 (2)
18	12Cr-4.5Al	12.2	8.0	11.5	8.8	10	20	130	2.37	–	–	0.0	–
19	12Cr-6Al	12.2	10.6	11.9	11.5	20	50	70	6.06	–	–	0.0	–
20	15Cr	16.0	0.0	13.3	1.0	40	20	70	3.32	29.0 (2.3)	1.2 (0.3)	2.2	44 (4)
21	15Cr-4Al	15.4	6.6	14.5	7.8	30	20	100	3.4	14.0 (1.5)	1.2 (0.3)	1.1	42 (3)
22	15Cr-8Al	14.7	14.2	13.6	15.7	40	10	150	4.07	2.2 (0.6)	1.2 (0.5)	0.2	29 (4)
23	17.5Cr	18.2	0.0	17.5	0.1	15	30	140	5.18	62.0 (3.1)	0.9 (0.3)	2.9	44 (5)
24	17.5Cr-3Al	17.9	5.7	14.4	6.9	25	15	100	1.76	28.0 (2.7)	1.2 (0.3)	2.6	46 (5)
25	17.5Cr-8Al	17.0	14.3	15.1	16.2	20	10	250	4.35	2.2 (0.7)	0.7 (0.0)	0.0	33 (5)
26	21Cr	21.8	0.0	19.5	0.3	20	15	160	4.4	76.0 (4.0)	1.0 (0.2)	3.6	53 (5)
27	21Cr-8Al	20.2	14.2	18.7	15.2	30	10	150	3.86	18.0 (2.0)	1.0 (0.1)	0.9	35 (2)
28	40Cr	38.8	0.0	37.8	2.6	–	–	–	–	–	–	–	–
8×10^{-4} **dpa/s**													
29	10Cr	10.7	0.0	10.4	0.3	–	–	–	–	6.8 (0.8)	1.1 (0.3)	0.5	28 (4)
30	10Cr-5Al	10.2	8.9	9.5	9.8	15	15	80	1.42	–	–	0.0	–
31	12Cr	12.9	0.0	12.8	0.1	30	30	150	10.4	0.7 (0.2)	1.8 (0.5)	0.2	24 (2)
32	12Cr-4.5Al	12.2	8.0	11.7	8.8	15	20	180	4.23	–	–	0.0	–
33	12Cr-6Al	12.2	10.6	11.0	11.7	10	20	160	2.47	–	–	0.0	–
34	15Cr	16.0	0.0	15.5	0.1	15	15	130	2.49	2.4 (0.9)	1.1 (0.2)	0.2	26 (3)
35	15Cr-4Al	15.4	6.6	13.9	7.9	15	30	200	6.7	–	–	0.0	–
36	15Cr-8Al	14.7	14.2	13.8	15.0	15	30	100	3.41	0.7 (0.4)	0.9 (0.1)	0.0	30 (2)
37	17.5Cr	18.2	0.0	16.9	0.1	20	10	230	3.53	32.0 (2.6)	0.8 (0.1)	0.9	47 (5)
38	17.5Cr-3Al	17.9	5.7	16.7	5.9	30	15	160	6.03	8.9 (1.1)	1.0 (0.1)	0.4	35 (4)
39	17.5Cr-8Al	17.0	14.3	15.8	15.4	20	10	130	2.22	–	–	0.0	–
40	21Cr	21.8	0.0	21.6	0.1	20	30	180	8.41	18.0 (1.3)	1.1 (0.1)	0.9	40 (4)
41	21Cr-8Al	20.2	14.2	19.1	15.2	20	15	200	5.15	8.8 (1.2)	1.0 (0.1)	0.4	34 (3)
42	40Cr	38.8	0.0	39.2	0.1	–	–	–	–	–	–	–	–

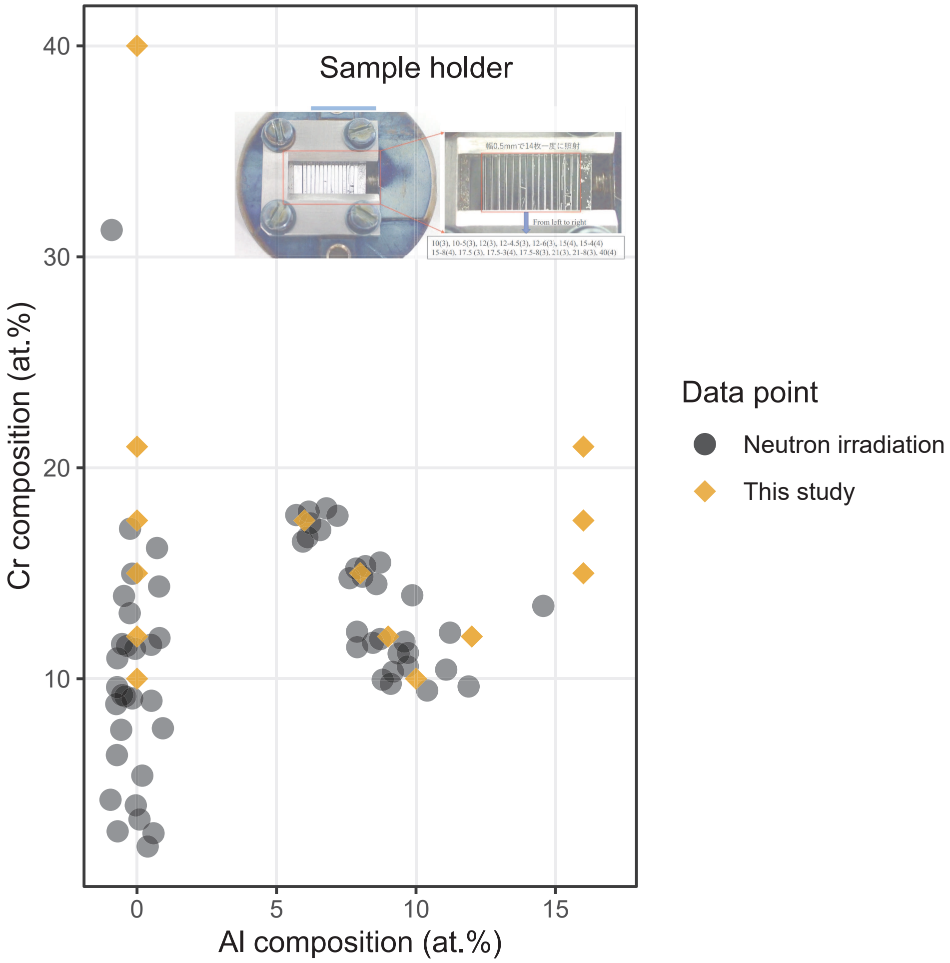

Figure 1: The relationship between the 14 alloy compositions selected, prepared, and used in this study and the alloy compositions in the neutron irradiation data from previous studies [6, 13–23]. The plot points of the neutron irradiation data were shifted vertically and horizontally around each data point using uniform random numbers of 1 at.% to avoid overlapping and indistinguishable data of the same composition. For the ion irradiation experiments, all prepared Fe–Cr–Al alloys were loaded into the same sample holder and irradiated simultaneously, as shown in the inset in the upper part of the figure.

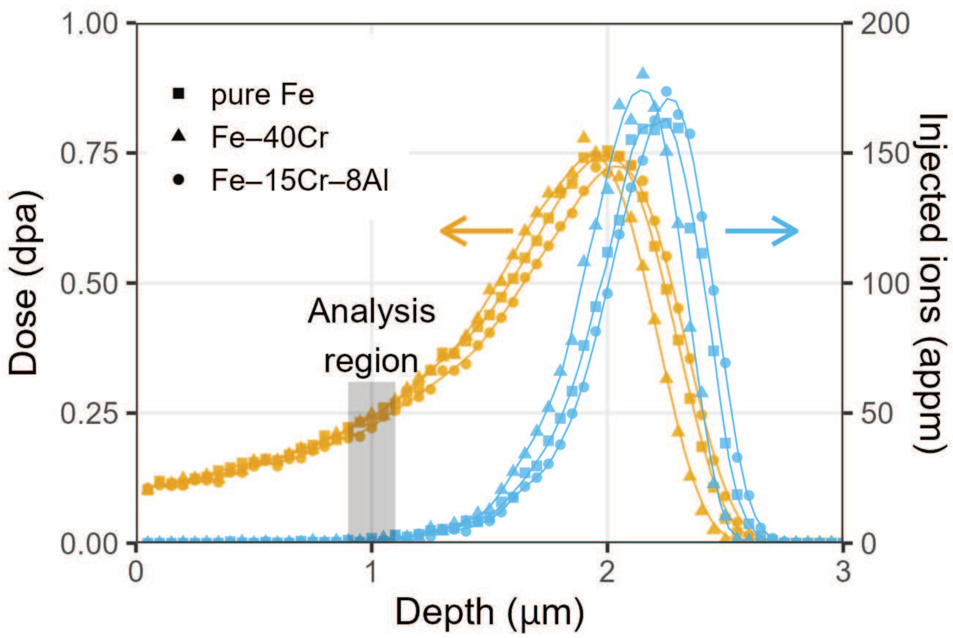

Figure 2: Depth profiles of displacement damage (left axis) and incident ion concentration (right axis) in pure Fe, Fe–40Cr, and Fe–15Cr–8Al (at.%) irradiated with 10.5 MeV Fe^{3+} ions based on SRIM calculations [24]. Following the calculation method proposed by Stoller et al. [25], which is widely accepted as the standard for dpa reporting, the "Quick Kinchin and Pease" option was used and 40 eV [26] was selected as the displacement threshold energy for Fe.

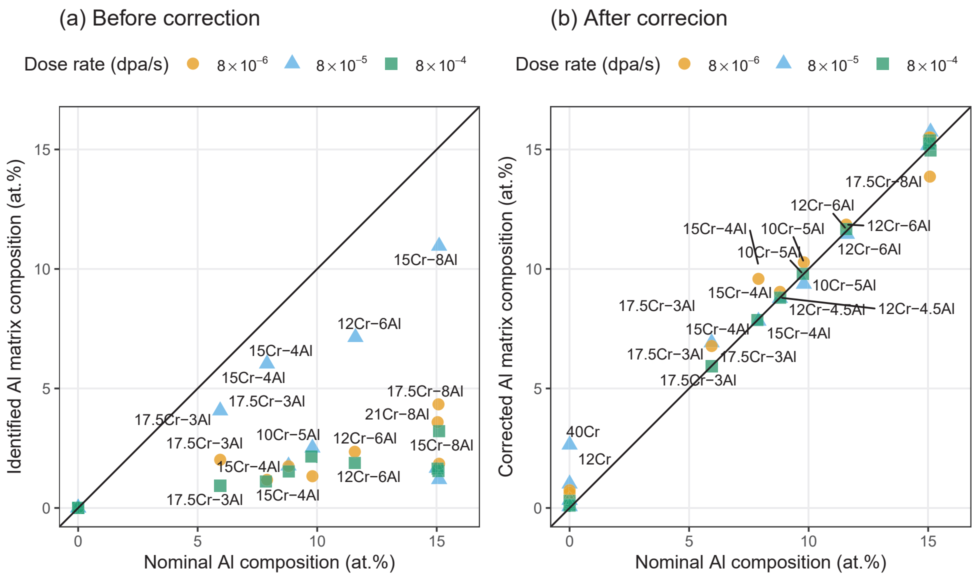

Figure 3: Identification of the Al matrix composition using 3DAP mass-to-charge ratios: (a) before correction, (b) after correction using natural isotope abundance ratios.

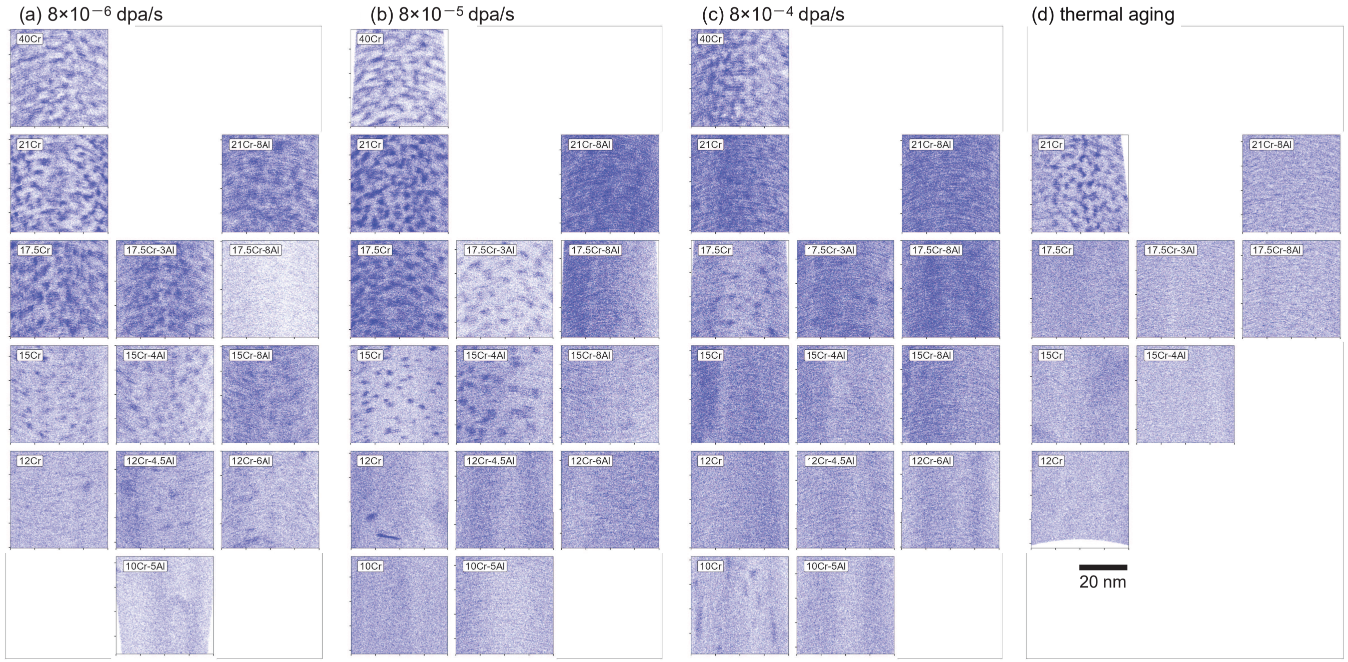

Figure 4: Mapping of Cr atoms by 3DAP analysis: (a) 8×10^{-6} dpa/s, (b) 8×10^{-5} dpa/s, (c) 8×10^{-4} dpa/s, and (d) thermal aging (samples taken from the masked part of the 8×10^{-5} dpa/s irradiated materials, corresponding to 50 min aging); the Cr atoms in an arbitrary volume of 40 nm square and 10 nm thick (5 nm thick for Fe–40Cr only) projected onto the square plane (point transmission rate 0.1). The order of each panel is the same as in Fig. 1, with a higher Al composition along the x-direction and a higher Cr composition along the y-direction. For Fe–10Cr in (a) 8×10^{-6} dpa/s, the data are missing due to sample destruction after fabrication for 3DAP analysis. For ease of reading, the alloy composition shown in the top left-hand corner of each panel is shown without the notation "Fe–", which is common to all.

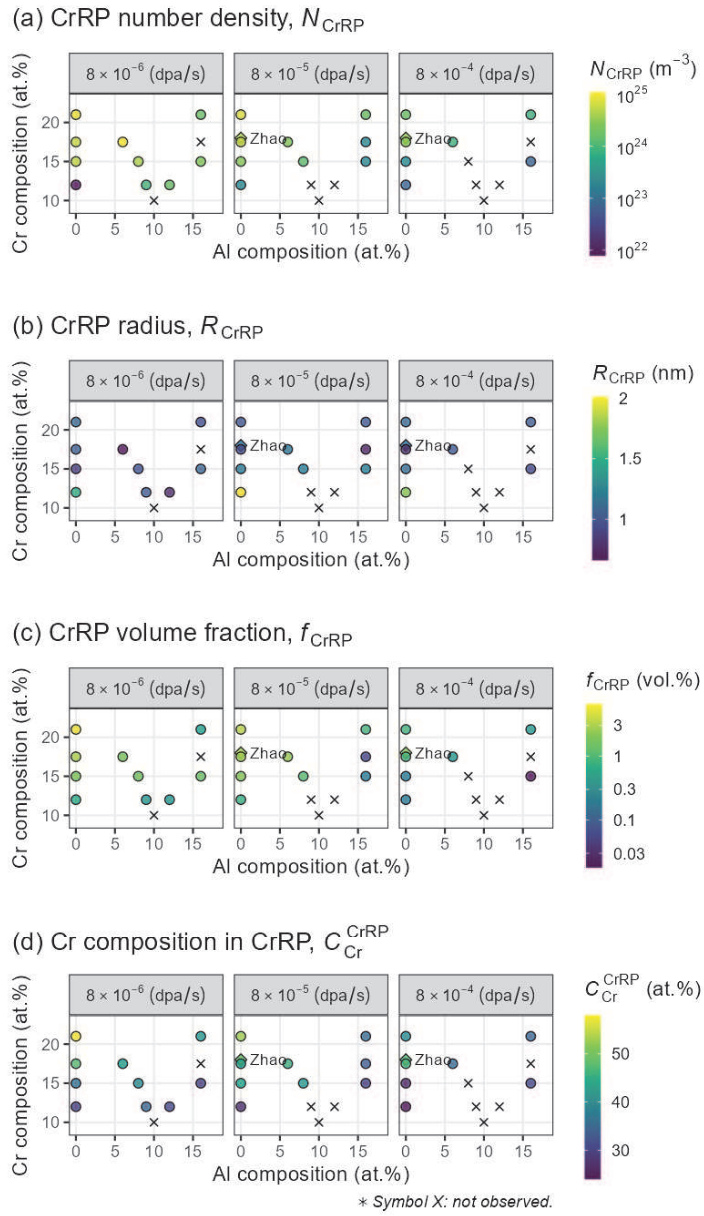

Figure 5: Cr and Al matrix composition dependencies of the measured quantities associated with CrRP in each Fe–Cr–Al alloy quantified by the clustering analysis: (a) CrRP number density, N_{CrRP}, (b) CrRP radius, R_{CrRP}, (c) CrRP volume fraction, f_{CrRP}, and (d) Cr composition in CrRP, $C_{\mathrm{Cr}}^{\mathrm{CrRP}}$. The $\times$ marks indicate data points where no CrRP formation was observed. Each panel is presented in ascending order from left to right for the three dose rates studied. Data for Fe–10Cr, which martensitises, and Fe–40Cr, which undergoes spinodal decomposition differently from other alloys, were excluded. The labelled diamond symbols correspond to Fe–18Cr data (at 350°C to 0.37 dpa at a damage rate of 10^{-3} dpa/s) from Zhao et al. [8].

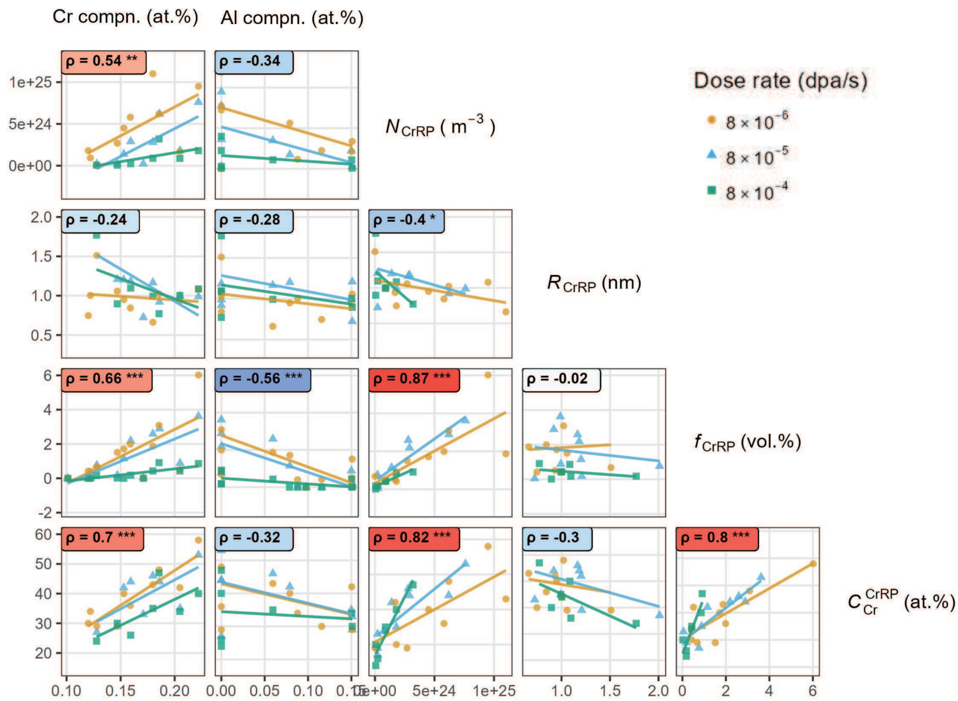

Figure 6: Correlation matrix between different CrRP-related quantities and variables (Cr and Al matrix compositions) obtained from the cluster analysis using the data as shown in Fig. 5. For the names of these quantities shown on the diagonal from top left to bottom right, the vertical and horizontal intersection panels show the correlation between the two corresponding quantities. Each panel shows a scatterplot and an approximate straight line for each dose rate. The upper left label of each panel shows Spearman's correlation coefficient ρ between the corresponding quantities, including the data for all dose rates, filled with a gradient such that the stronger the negative correlation, the darker the blue and the stronger the positive correlation, the darker the red. The symbol to the right of each correlation coefficient indicates the level of significance based on the p-value calculated from the correlation test as follows: no symbol: not significant, . : $p < 0.10$, *: $p < 0.05$, ***: $p < 0.01$, ***: $p < 0.001$.

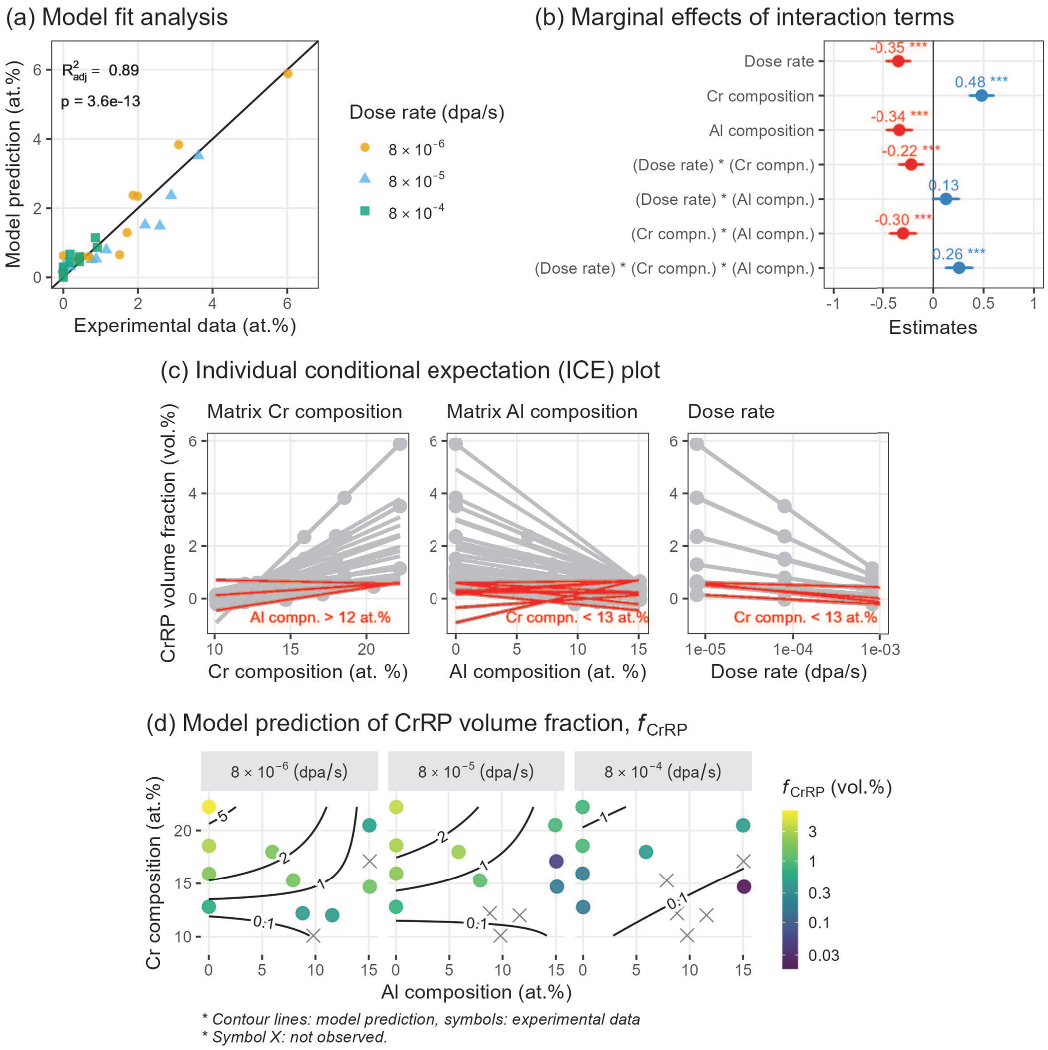

Figure 7: Assessment of the influence of each variable and their interactions on the CrRP volume fraction using multiple regression model. (a) Scatter plot comparing the experimental values of CrRP volume fraction (horizontal axis) and the estimated values from the multiple regression model (vertical axis). (b) Forest plot of the average marginal effect of each explanatory variable on the change in CrRP volume fractions, including interactions in the multiple regression model. Explanatory variables corresponding to positive or negative effects on the CrRP volume fraction are marked with a significance star and a bar for the 95% confidence interval. (c) Individual conditional expectation (ICE) profiles showing how the predicted values (lines) of individual measurements (symbols) vary as a function of the given explanatory variables. The red lines are drawn to highlight the presence of interactions where the effect of each explanatory variable on the CrRP volume fraction depends on the composition of Cr and Al. (d) The relationship between measured values and contours of the CrRP volume fraction drawn based on the prediction from the multiple regression model at 100 × 100 grid points in the compositional range of Cr and Al.

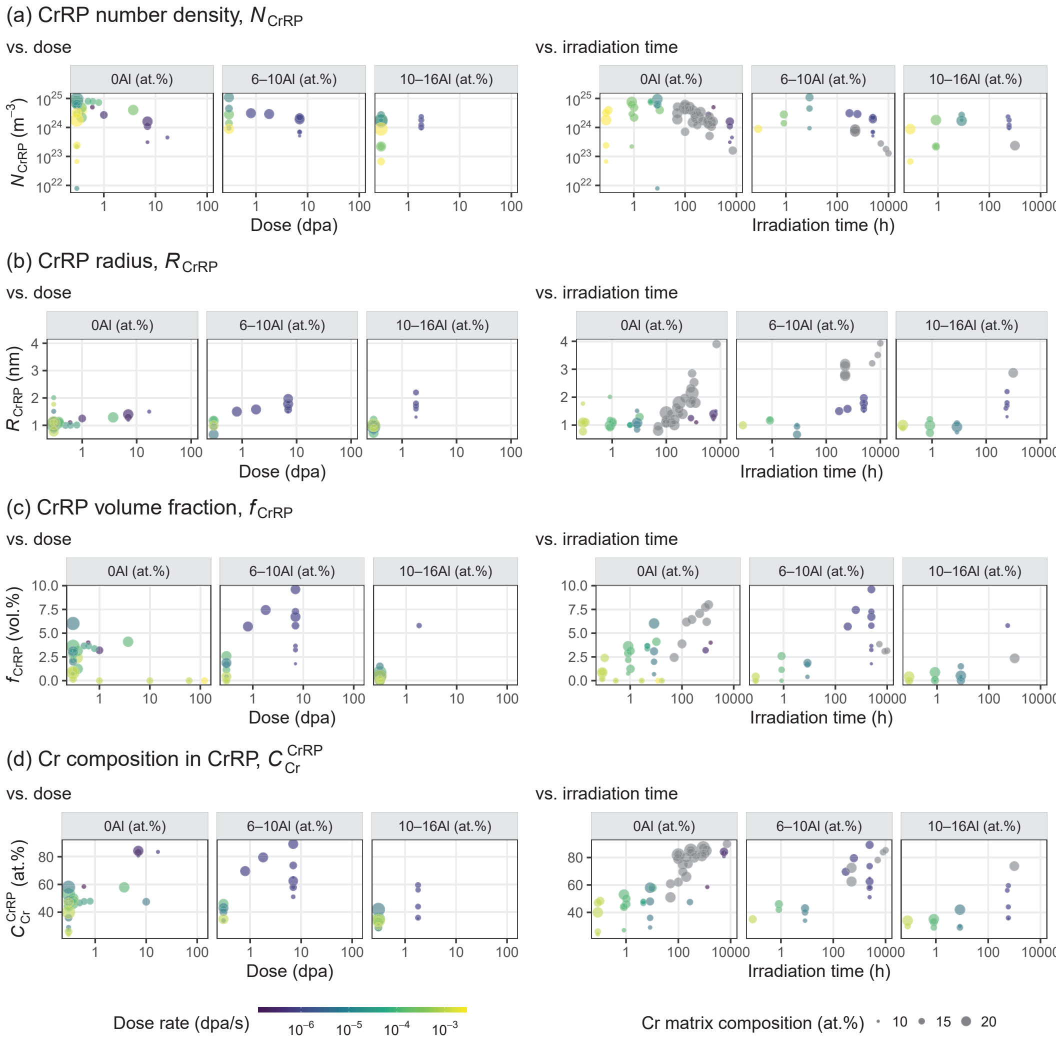

Figure 8: For the various CrRP-related measurements: (a) CrRP number density, (b) CrRP radius, (c) CrRP volume fraction, and (d) Cr concentration in CrRP, the three figures in the left column show the dose dependence and the three figures in the right column show the irradiation time dependence, all on a logarithmic scale on the horizontal axis. Each set of three figures is arranged in ascending order from left to right regarding the range of the Al compositions (at.%). The size of the plot points represents the magnitude of the Cr composition, and the colour represents the dose rate. For comparison, the data obtained in this study (350°C), but also previously reported self-ion irradiation data (300°C–350°C) [8, 11–13] and neutron irradiation data (300°C–390°C) [6, 7, 17, 19, 21–23] are plotted. In the irradiation time dependence plots in the right column, data for thermal aging (gray points), which can be assumed to be the limit of the zero dose rate, are plotted to compare irradiation effects. However, since there is little thermal aging data below 450°C, the data for 475°C and 500°C [7, 8, 27, 34–38] are plotted for reference, although the temperature range differs from the irradiation data.